Separation and Purification Technology 395 (2026) 137736

Contents lists available at ScienceDirect

Separation and Purification Technology

journal homepage: www.elsevier.com/locate/seppur

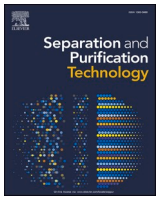

Impact of freeze drying on pore size distribution of amorphous silica membranes derived from gas permeation activation energies

Tanzila Anjum [a], Tian Heng Qin [b], Gianni Olguin [c,*], Yinxiang Wang [a], Dongkuan Zhang [a], Xiaonan Kou [a], David K. Wang [d], Xiaozhen Zhang [e], Bradley Ladewig [f], Asim Laeeq Khan [g], Guozhao Ji [a,*]

[a] Key Laboratory of Industrial Ecology and Environmental Engineering, School of Environmental Science and Technology, Dalian University of Technology, Dalian 116024, PR China
[b] School of Engineering, University of Aberdeen, Aberdeen AB24 3UE, UK
[c] Pontificia Universidad Católica de Valparaíso, Escuela de Ingeniería Química, Valparaíso, Chile
[d] School of Chemical and Biomolecular Engineering, The University of Sydney, New South Wales 2006, Australia
[e] School of Materials Science and Engineering & Key Laboratory of Inorganic Membranes, Jingdezhen Ceramic University, Jingdezhen 333403, PR China
[f] Paul Wurth Chair, Faculty of Science, Technology and Medicine, University of Luxembourg, 2, Avenue de l'Université, L-4365 Esch-sur-Alzette, Luxembourg
[g] Department of Chemical Engineering, Faculty of Engineering, Islamic University of Madinah, Madinah 42351, Saudi Arabia

ARTICLE INFO

Keywords:
Activated transport
Microporous structure
Siloxane ring distribution
Gas separation membranes
Hydrogen separation
Knudsen diffusion

ABSTRACT

Microporous silica membranes have enormous potential to contribute to clean-energy applications by H_2 separation, yet their separation performance is severely constrained by the presence of membrane pore defects due to traditional thin-film drying techniques. In this work, a mathematical modeling approach based on activation energy derived from empirical measurement of membrane gas permeation is proposed to quantitatively estimate the pore size distribution of amorphous silica membranes prepared by freeze-drying, demonstrating a synthesis-structure-transport property correlation. The synthesis of cobalt-doped silica membranes was performed through evaporation drying and freeze drying, and the membranes were tested using He and N_2 single-gas permeation at 200–500 °C. Apparent activation energies were determined using an activated transport assumption based on the Oscillator model and Effective Medium Theory (EMT) to estimate the relative roles of siloxane ring sizes in the amorphous silica network. The reconstructed pore size distribution was validated by the modeled activation energies and gas permeances that were in close agreement with the experimental values. The results showed that freeze-dried membranes had a higher percentage of 5- and 6-membered rings (98.5% collectively) and a reduced contribution of larger rings, which suggests a more compact and homogeneous microporous structure. These findings indicate that freeze drying can effectively regulate the pore structure of silica membranes and that activation-energy-based analysis is an effective method to determine the pore size distribution of amorphous silica membranes.

1. Introduction

The global targets of sustainability and low-carbon energy systems for major industries have boosted the economic interest in H_2 as a clean and versatile energy carrier [1,2]. Even though the technological use of methane steam reforming has been the common practice to manufacture H_2 [3], the gas streams that are generated have to undergo an efficient purification process to eliminate the content of CO_2, N_2, and other by-products [4,5]. Microporous silica membranes are an appealing alternative to traditional purification technologies [6] because of their low material and processing cost, structural tunability, low energy expenditure, compact system construction, and high-temperature compatibility [7,8].

To achieve efficient gas transport in microporous membranes, it is crucial to understand and control the pore size distribution of the amorphous silica network during the manufacturing process [9]. Silica matrix is a disordered network of interconnected siloxane (Si–O–Si) basic units with sub-nanometer pores that can selectively discriminate

* Corresponding authors.
E-mail addresses: gianni.olguin@ucv.cl (G. Olguin), guozhaoji@dlut.edu.cn (G. Ji).

https://doi.org/10.1016/j.seppur.2026.137736
Received 9 February 2026; Received in revised form 23 March 2026; Accepted 24 March 2026
Available online 24 March 2026

gas molecules with different kinetic diameters [10]. In narrowly distributed pores in the molecular sieving regime, small gases like H_2 and He are selectively permeated, and larger or more strongly adsorbing molecules experience limited gas transport [11]. In molecular sieving, permeation is dominated by activated diffusion, and gas permeance tends to increase with temperature [12]. The transport mechanisms, like Knudsen diffusion or viscous flow, can, however, play a role in reducing selectivity when the pore size distribution becomes broadened due to larger voids [13]. Although Knudsen diffusion offers limited selectivity, viscous flow is non-selective; thus, it is imperative to have a small and tight microporous network to facilitate high selectivity in silica membranes [14].

On an atomic scale, amorphous silica pore structure is based on the structure of the tetrahedra of SiO_4 linked to each other by shared oxygen atoms [15]. The fundamental Si—O bond lengths and interior O–Si–O angles are closely similar to those of crystalline silica, but due to the lack of long-range order, the structure becomes highly disordered [16,17]. The differences in the number of Si–O–Si bonds cause the formation of siloxane rings of dissimilar sizes that cumulatively determine the effective pore sizes of the membrane [18]. These rings may be of various members of interconnected tetrahedra, either as few as a three-membered ring or larger multi-membered structures [19]. Five- to nine-membered rings are usually recognized as the most common ring types within amorphous silica membranes, as they create sub-nanometer apertures (Fig. 1). Previous structural studies have revealed that the effective pore sizes of amorphous silica membranes increase with ring sizes. For instance, according to the geometries of 4–8-membered siloxane rings, the distance from the ring-center to the oxygen atom is approximately 0.191, 0.228, 0.265, 0.304, and 0.344 nm, respectively, showing that the diffusion apertures are progressively increasing within the silica network. These geometrical properties offer the structural basis to correlate siloxane ring size with the effective transport apertures in amorphous silica membranes [20]. The relative proportion of these ring populations within the silica network creates the available pore structure, hence decisively governs permeation behavior, selectivity, and transport phenomena.

The fabrication pathway is a key factor in determining the resulting pore structure of silica membranes. The sol-gel process has become one of the most common synthesis methods, especially because of the low cost, compositional versatility, and molecular-level capability to modify the silica network [21]. In a typical sol-gel route, a porous support is dip-coated with a silica precursor solution, dried, and then subjected to calcination to form the membrane [22]. The drying stage is a crucial step in the fabrication of the membranes, as during this stage, the structural evolution of the silica network mainly occurs. During traditional evaporation drying, the solvent is removed from liquid-vapor interfaces, and this results in the creation of capillary forces due to the surface tension that causes the fragile silica network to experience a high level of mechanical stress [23]. This stress can induce shrinkage and structural rearrangement of the silica network, causing the pore collapse, or the development of cracks or pinholes [24], eventually compromising the structural integrity and membrane selectivity. Conversely, after the membrane has been dried and the silica structure has solidified, further high-temperature calcination can largely facilitate condensation reactions of silanol groups (Si–OH) to produce siloxane bonds (Si–O–Si), causing the stabilization and slightly condensing the structure. There are no liquid-vapor interfaces formed during the calcination, and therefore, there are no capillary stresses, and the structural changes are dominated by the solid-phase reactions and not extensive pore restructuring.

To overcome the limitations associated with conventional drying, our previous study investigated freeze-drying as a viable approach to minimize the defects caused by surface tension during the drying process [25]. Unlike evaporation drying, the freeze-drying approach eliminates the solvent via sublimation. In this process, the membranes undergo rapid freezing followed by solvent removal in the solid state under vacuum, avoiding capillary stresses and structural deformation of the silica matrix [26]. Rapid freezing through liquid nitrogen promotes the formation of small ice crystals and inhibits phase separation, leaving a finer, more homogenous pore structure after sublimation [27]. In our recent freeze-drying investigation, it was established that freeze-dried silica membranes have far fewer microporous defects and are better at small gas separation as compared to evaporation-dried silica membranes. These advancements have been credited to high structural integrity, low density of silanol groups that form tighter pore structures [25]. However, in spite of these promising experimental results, quantitative insight into the effect of freeze drying on the pore size distribution of amorphous silica membranes remains limited.

Determining pore size distribution in sub-nanometer silica membranes proves to be very challenging. Traditional methods like nitrogen-physi-sorption [28] are usually ineffective since the N_2 molecules fail to reach the tiniest pores in dense silica networks. Conventional Transmission Electron Microscopy (TEM) techniques have limited capability to resolve such extremely small (<1 nm) and highly disordered microporous structures. Other characterization techniques, such as nano-

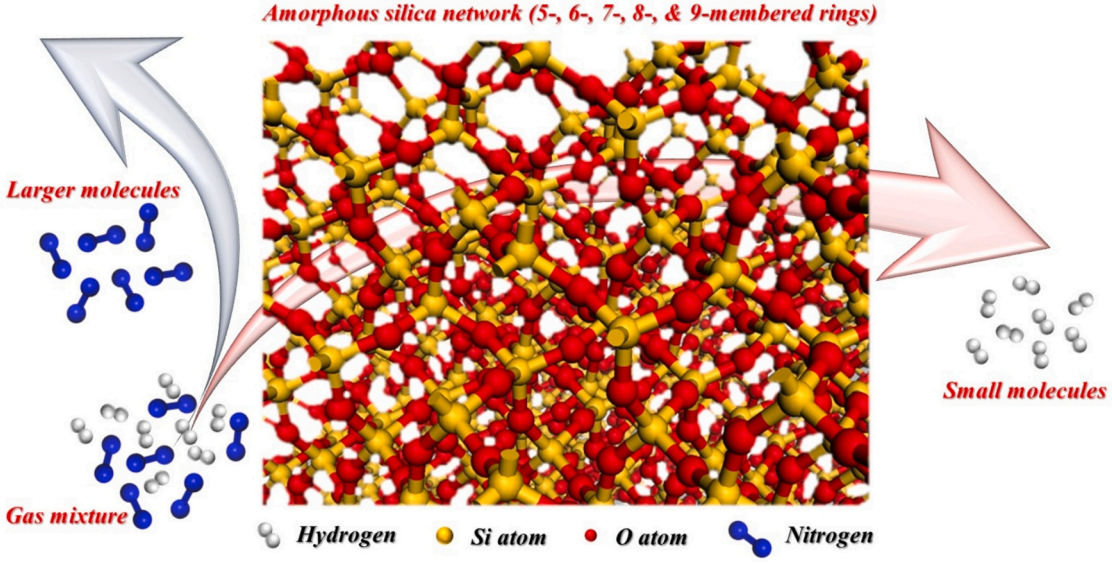

Fig. 1. Schematic of the amorphous silica network formed by siloxane rings with hydroxyl terminations.

permporometry [29] and positron annihilation lifetime spectroscopy (PALS) [30,31], offer valuable insights into pore structure but involve complex experimental systems, specialized instrumentation, and sample processing limitations that can limit their application for thin film membranes. This leads to an increased interest in indirect methods that determine pore size distribution based on gas transport behavior [32]. Gas permeation measurements offer an effective and non-destructive way of investigating the nature of the membrane structure, especially when analyzed by relevant transport models [33]. The apparent activation energy of gas transport among the parameters obtained by carrying out permeation experiments is particularly important. The apparent activation energy, unlike permeance, is determined by the inherent properties of gas molecules and the pore network, rather than the thickness of the membrane and experimental conditions. It depends mainly on the size of the permeating species and the interaction potential within the pores. As a result, activation energy is relatively independent of uncertainties in membrane thickness and provides a powerful parameter to measure the pore size distribution [34].

The pores in amorphous silica membranes can be modeled as a distribution of siloxane rings of varying sizes, which are associated with a specific pore dimension. Through the sufficient correlation of the experimentally obtained activation energies and the modeled energy values given to each ring size, a reconstruction of the pore size distribution that most accurately predicts the real structure of the membrane can be deduced. This activation-energy-mechanism method offers a physically sensible and computationally efficient mode of connecting membrane structure with transport characteristics. It has been proven in previous modeling research that this concept can be applied and is practicable [34,35], but the technique has not been extended to gain insight into calculating the pore size distribution of silica membranes as a comparative study to investigate differences in drying methods.

This paper presents an experimental and modeling study that examines the size distribution of pores in amorphous silica membranes produced by freeze drying and conventional drying. Cobalt-doped silica membranes were prepared by employing the conventional evaporation drying and freezing drying to investigate the effect of drying methods on the structure of silica membranes. Single-gas permeation experiments from 200 to 500 °C were conducted to determine apparent activation energies of He and N_2. These experimentally obtained values were further used as inputs in an activated transport model to reconstruct the pore size distribution of the amorphous silica network. The modeled and experimental activation energies and permeances were compared systematically to validate the reconstructed pore networks of the silica membranes. The current research explains how freeze drying alters the pore structure of amorphous silica membranes and provides a strong framework for determining the size distribution of pores in microporous membranes through a combination of both experimental and modeling processes.

2. Methodology

2.1. Experimental

The detailed description of experimental methodology has been reported in our previous study [25]. A cobalt-doped silica sol was prepared using tetraethyl orthosilicate (TEOS) as the silica precursor, distilled water as the hydrolysis agent, absolute ethanol as the solvent, hydrogen peroxide (H_2O_2) as the oxidizing agent, and cobalt nitrate hexahydrate ($Co(NO_3)_2.6H_2O$) as the cobalt source for enhancing membrane hydrothermal stability. The components were combined at a molar ratio of 4:200:170:9:0.4, respectively. Initially, distilled water and ethanol were mixed with $Co(NO_3)_2.6H_2O$ under vigorous stirring until complete dissolution was achieved. The solution was then cooled to ≤5 °C, after which H_2O_2 and TEOS were introduced dropwise in sequence. The resulting mixture was continuously stirred for 5 h to promote controlled hydrolysis and condensation reactions, yielding a homogeneous Co-silica sol. Two cobalt-doped silica membranes were fabricated, one of which was prepared by using the traditional evaporation drying method, and the other utilized a customized freeze-drying method. They were both prepared on MFI nanosheet intermediate layer coated on α-alumina tubular supports via the dip-coating technique. Each coating cycle involved dipping the substrates vertically in the precursor sol at a rate of 0.33 mm/s. The substrates were withdrawn at the same constant speed after 1 min to ensure the complete wetting of the substrates. The evaporation-dried membrane was left undisturbed in ambient conditions for 10 min.

Conversely, the membrane to be freeze-dried was quickly frozen by placing the freshly coated support into a Teflon container and putting it in liquid nitrogen for 20 min. The frozen sample was then put into a freeze-dryer and allowed to undergo low-pressure (<10 Pa) sublimation at a condenser temperature of −50 °C for 24 h. Each of the deposited layers was then calcined separately in a vertical tubular furnace, irrespective of the drying method. The calcination was carried out at 600 °C for 2.5 h at a heating and cooling rate of 1 °C/min. The six cycles of coating-calcination were repeated to achieve the final thickness of the membranes. The membranes were then assessed for single gas permeation performance within a custom-designed permeation rig. The membrane module was placed in a furnace with a controlled temperature, and the end sealing was done by using leak-tight stainless-steel fittings fitted with graphite ferrules. Helium (He) and nitrogen (N_2) were used as test gases to determine membrane transport properties at a temperature between 200 and 500 °C and at a transmembrane pressure difference of 500 kPa. The use of He (kinetic diameter 2.6 Å) instead of H_2 (2.89 Å) was due to the laboratory safety limits, whereas N_2 (3.64 Å) was selected as a representative larger gas because its kinetic diameter approximates those of other relevant gases, including Ar (3.40 Å), CO_2 (3.30 Å), CO (3.76 Å), and CH_4 (3.80 Å), allowing evaluation of diffusion resistance and pore size characteristics of the membranes.

A bubble flow meter was used to measure the flow of gas on the permeate side and to measure the temperature-dependent permeance of each gas. For each drying method, three membranes were independently fabricated and tested to ensure reproducibility. For every membrane sample, multiple permeance measurements were collected at each temperature, and the reported values correspond to the average of these measurements.

2.2. Modeling

As is known, the micro-structure determines the transport of gas molecule in the silica matrix; in turn, molecular transport determines the permeation data, and the permeation data determines the activation energy. The different activation energies measured in the permeation experiments originate from the differences in the structure. Therefore, there is a correspondence between the microstructure and the activation energy. This model will follow the above order and establish this correspondence. The purpose of the model is to establish a quantitative link between experimentally measurable transport properties and the effective structural features that control gas diffusion in the membrane.

2.2.1. Kinetic model for activated gas permeation

Amorphous silica is typically permeable to light gases (e.g., H_2, He) through a thermally activated transport pathway [36,37]. The molar flux (J) in the membrane gas separation is caused by the difference in transmembrane pressure (ΔP) and presents a reverse relationship with membrane thickness (L), which can be expressed as in Eq. 1. The flux can further be formulated under Fick's law of diffusion (Eq. 2), with the velocity of transport being controlled by a diffusion coefficient (D) and concentration gradient (c) across the membrane [38].

$$J = \frac{P}{L}\Delta p \tag{1}$$

$$J = -D\frac{dc}{dx} \tag{2}$$

To understand dilute adsorption in microporous solids, it is convenient to describe the concentration of adsorbed molecules in terms of gas pressure by Henry's law as follows:

$$c = Kp \tag{3}$$

The temperature dependence of the Henry constant (K) satisfies the Van't Hoff relation, with Q_{st} representing the isosteric heat of adsorption [13]:

$$K = K_0 \exp\left(\frac{Q_{st}}{RT}\right) \tag{4}$$

A common Arrhenius expression (Eq. 5) of temperature variation is used to describe the temperature dependence of diffusion, where D_0 is a pre-exponential factor, and E_m is the migration barrier between adjacent sorption positions.

$$D = D_0 \exp\left(\frac{-E_m}{RT}\right) \tag{5}$$

The combination of Eqs. 2 to 5 gives the temperature-dependent flux expression in Eq. 6:

$$J = D_0 K_0 \exp\left(\frac{Q_{st} - E_m}{RT}\right)\frac{\Delta p}{L} \tag{6}$$

This expression provides directly an apparent permeation activation energy, denoted in Eq. 7, in which the adsorption and migration terms are interrelated:

$$E_a = E_m - Q_{st} \tag{7}$$

A rearrangement of Eq. 1 leads to the expression of permeance, expressed in Eq. (8); an application of logarithmic transformation then leads to Eq. 9, used to extract the activation energy E_a, by plotting the graph on an Arrhenius-type plot.

$$\left(\frac{P}{L}\right) = \frac{D_0 K_0}{L}\exp\left(-\frac{E_a}{RT}\right) \tag{8}$$

$$\ln\left(\frac{P}{L}\right) = \ln\left(\frac{D_0 K_0}{L}\right) - \frac{E_a}{RT} \tag{9}$$

Sign of E_a can either be positive or negative, depending on the comparison of the adsorption and mobility contributions. When E_a is positive, it means that flux rises with temperature, and when E_a is negative, it means flux falls with temperature. Notably, the differentiation of Eq. 9 results in Eq. 10, thus illustrating that E_a does not depend on the membrane thickness, because L is constant, which leads to $d(\ln L)/d(-1/RT) = 0$. Thus, E_a is considered a natural characteristic of the membrane gas system.

$$E_a = \frac{d\left[\ln\left(\frac{P}{L}\right)\right]}{d\left(-\frac{1}{RT}\right)} = \frac{d(\ln P - \ln L)}{d\left(-\frac{1}{RT}\right)} = \frac{d(\ln P)}{d\left(-\frac{1}{RT}\right)} - \frac{d(\ln L)}{d\left(-\frac{1}{RT}\right)} = \frac{d(\ln P)}{d\left(-\frac{1}{RT}\right)} \tag{10}$$

2.2.2. Potential in silica nanopores

An important step in the Oscillator model is obtaining the potential field inside the pore [39]. The potential depends on the pore size and Lennard-Jones (L-J) parameters. The L-J kinetic diameter (σ) modulates gas diffusion in silica nanopores, but solubility is mainly determined by affinity to adsorption, commonly the Lennard-Jones well depth (ε) of gas-solid interactions [40].

Pore-scale diffusion was analyzed using the Oscillator model defined by Bhatia et al. [41], which accounts for fluid-wall interactions of the gas molecules through nanopores:

$$D = \frac{2}{\pi m \int_0^\infty r e^{-\frac{\varphi(r)}{k_B T}} dr}\int_0^\infty e^{-\frac{\varphi(r)}{k_B T}} dr \times \int_0^\infty e^{-\frac{p_r^2}{2mk_B T}} dp_r \int_0^\infty e^{-\frac{p_\theta^2}{2mr^2 k_B T}} dp_r \int_{r_{co}(r,p_r,p_\theta)}^{r_{c1}(r,p_r,p_\theta)} \frac{dr'}{p_r(r', r, p_r, p_\theta)} \tag{11}$$

To infer the contribution of gas-pore wall interaction to sub-nanometer separations, the intermolecular potential is characterized by the L-J expression in Eq. 12, where φ denotes the interaction potential, and $r_{a\text{-}a}$ is the separation between atomic centers.

$$\varphi(r_{a-a}) = 4\varepsilon_{ij}\left[\left(\frac{\sigma_{ij}}{r_{a-a}}\right)^{12} - \left(\frac{\sigma_{ij}}{r_{a-a}}\right)^{6}\right] \tag{12}$$

To determine the Lennard-Jones parameters of cross interactions, the Lorentz-Berthelot mixing rules are used to derive them [42,43]. The parameter set used in this paper is summarized in Table 1 [39].

$$\varepsilon_{ij} = \sqrt{\varepsilon_i \varepsilon_j} \tag{13}$$

$$\sigma_{ij} = \frac{(\sigma_{ij} + \sigma_{ij})}{2} \tag{14}$$

Having the Lennard-Jones parameters (Table 1) and mixing compositions (Eqs. 13 and 14), the interaction potential between the gas and the pore wall was obtained in both He and N_2 in silica pores made of 5–9-membered rings.

To characterize geometric confinement within the amorphous silica network, pore sizes were modeled using characteristic diameters of 5–9-membered rings of siloxane as represented in Table 2. These pore sizes are in the sub-nanometer range, which is important in molecular sieving of silica membranes. This ring-based representation offers a structural connection between pore geometry and gas transport behavior, where the transport-controlling network essentially consists of siloxane (Si–O–Si) linkages, with a limited number of Si–OH groups, which can be found after calcination. These residual silanol groups are actually the terminated sites and may influence the adsorption behavior. However, their contribution to overall transport is minimal and is inherently reflected in the permeance-temperature relation and activation energy analysis.

Fig. 2a compiles the computed central potential versus pore size, and Figs. 2(b-f) show the radial profiles of potential across the individual pore geometries, as formulated by Ji et al. [35]. Within the smallest pores, which consist of 5 and 6-membered rings, the field of interaction is characterized by a strong repulsion near the pore wall, thus creating extremely undesirable energetic conditions for the larger-sized molecules. As the pore size increases (7–9-membered rings), the repulsive contribution decreases, allowing a deeper potential well to form, which reflects a pore environment where attractive interactions dominate and allow the easy accommodation of molecules. The following assessment of adsorption and transport parameters used in the pore-network calculations relies on these potential landscapes.

The adsorption equilibrium constant (K) of He and N_2 for each pore family was then calculated in the range of 200–500 °C (see Table 3). The data show very weak adsorption in the relatively smaller pores, particularly for He (3.18×10^{-4}) and N_2 (4.77×10^{-61}) in the 5-membered ring, where K is negligible throughout the temperature range. This finding is consistent with the strong exclusion expected in the presence of strong repulsive intermolecular forces. Conversely, bigger pores have much higher K values that are explicitly temperature dependent. These

Table 1
Lennard-Jones parameters used in the transport model.

Parameter	He	N_2	O
σ (nm)	0.26	3.798	0.27
ε/k_B (K)	10.22	71.4	230

Table 2
Characteristic pore diameters of siloxane ring structures in amorphous silica.

Rings	Diameter (Å)
5-membered ring	4.558
6-membered ring	5.306
7-membered ring	6.076
8-membered ring	6.886
9-membered ring	7.720

K values decrease with temperature across the 7–9-membered rings, which is as expected of thermally weakened adsorption. Such pore- and temperature-dependent *K* values are used directly as inputs in the determination of pore-level conductance in the activated transport model. Simultaneously, the diffusion coefficient (*D*) of He and N_2 in each of the pore sizes at 200–500 °C was obtained (see Table 4). The calculated *D* values grow gradually with temperature and pore diameter, corresponding to decreased confinement and an increase in molecular mobility in the larger pores. Both He and N_2 gases show an increase in diffusivity with pore size and temperature, while the former is much higher than the latter, which is in accord with its smaller kinetic

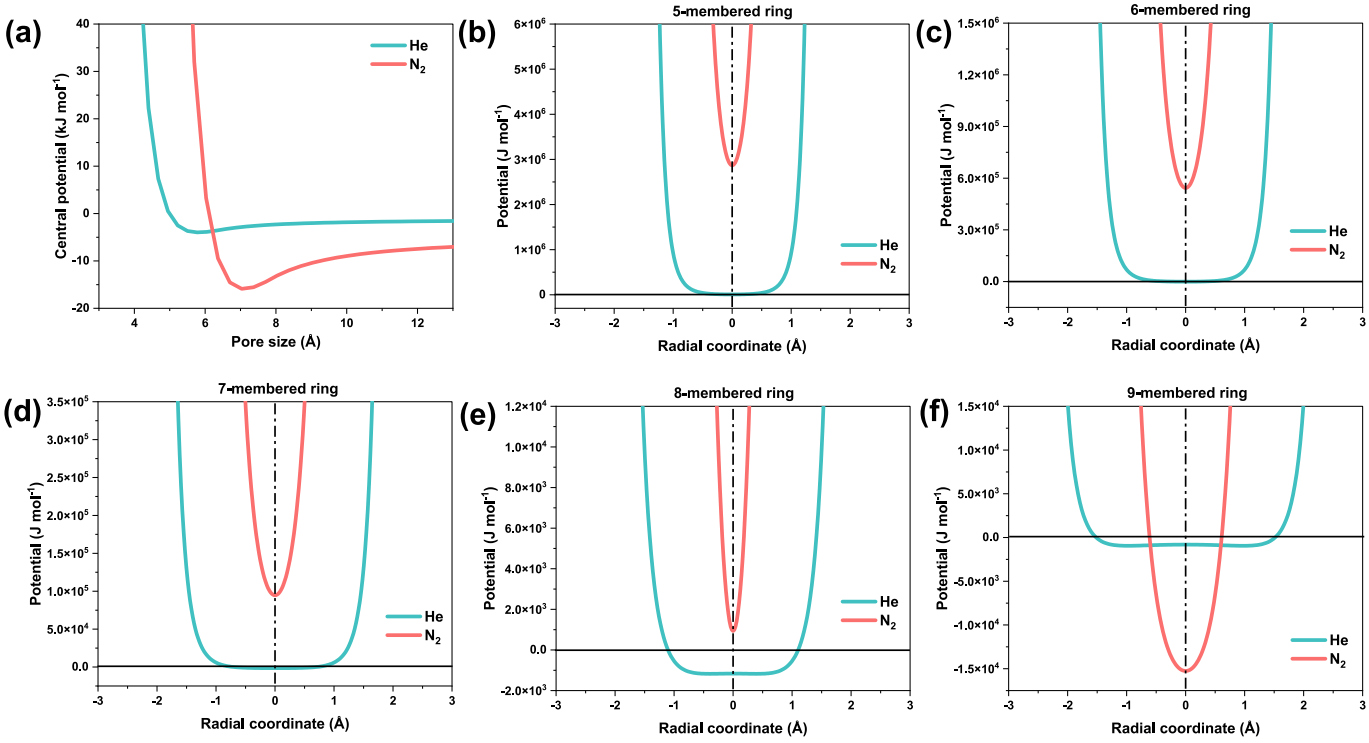

Fig. 2. (a) Variation of the central potential of He and N_2 as a function of silica pore size; (b-f) distribution of gas-silica interaction potential within pores of different sizes (positive and negative values correspond to repulsive and attractive interactions, respectively).

Table 3
Adsorption equilibrium of He and N_2 in pores of different sizes at various temperatures.

Rings	Adsorption equilibrium *K*							
	200 °C		300 °C		400 °C		500 °C	
	He	N_2	He	N_2	He	N_2	He	N_2
5-membered ring	3.50×10^{-5}	3.53×10^{-97}	9.20×10^{-5}	6.06×10^{-81}	1.86×10^{-4}	1.60×10^{-69}	3.18×10^{-4}	4.77×10^{-61}
6-membered ring	4.14×10^{-2}	1.88×10^{-16}	3.98×10^{-2}	3.47×10^{-14}	3.93×10^{-2}	1.39×10^{-12}	3.94×10^{-2}	2.19×10^{-11}
7-membered ring	0.1817	0.02417	0.1569	0.0197	0.143	1.75×10^{-2}	0.1345	1.62×10^{-2}
8-membered ring	0.2943	5.292	0.2572	2.089	0.2356	1.106	0.2218	0.6982
9-membered ring	0.3717	7.849	0.3321	3.391	0.3083	1.899	0.2928	1.244

Table 4
Diffusion coefficients of He and N_2 in pores of different sizes at various temperatures.

Rings	Diffusion coefficient *D* ($m^2\ s^{-1}$)							
	200 °C		300 °C		400 °C		500 °C	
	He	N_2	He	N_2	He	N_2	He	N_2
5-membered ring	13.85	1.029	16.66	1.247	19.38	1.468	22.1	1.69
6-membered ring	32.84	2.688	38.7	3.261	44.37	3.817	49.77	4.405
7-membered ring	63.5	6.397	73.11	7.691	82.24	8.978	90.85	10.22
8-membered ring	102.1	14.23	115.7	16.8	128.6	19.26	140.7	21.63
9-membered ring	131.4	28.24	149.5	32.34	166.3	36.2	182.2	39.88

diameter and weaker attraction toward the pore wall. Note that the obtained necessary temperature-dependent adsorption and diffusion inputs ($K(r_p)$, $D(r_p)$), in Tables 3 and 4, can be, in turn, fed into the pore-network transport calculations in the next section.

2.2.3. Transport phenomena in nano-porous networks

One of the challenges in using diffusion theory to microporous materials is that the process of transport is controlled not by individual pores, but by a network in the sense of pore connectivity and differing size distributions of pores. In order to determine the overall permeation behavior using such nano-porous media, transport at the pore scale is initially defined, and then it is further extended to the network level. The Oscillator model in this study is applied at the level of an individual pore, and we assume a stochastic, interconnected network of pores in which each junction is characterized by a coordination number, N, the number of pores meeting at an intersection. The value of N is assumed to be constant across the network. This is then applied to the disordered network with pores having a homogenized conductance to obtain the approximate value, using effective medium theory (EMT) [44].

Permeation (mol/s) across the pore radius (r_p) is dominated at the pore level by a pseudo bulk pressure gradient (P), defined by Eq. 15, where l is the pore length. The equilibrium constant, $K(r_p)$, is calculated based on the hypothesis of local thermodynamic equilibrium of the nanoscale, which results in the formula given in Eq. 16. Value of pore diffusivity $D(r_p)$ is then determined using the oscillator model (Eq. 6). A combination of these expressions gives the pore conductance (λ) as found in Eq. 17. With effective medium theory (EMT), the effective conductance (λ_e) due to an array of pores can be calculated using Eq. 18, and hence the bulk permeate flux, expressed in Eq. 19, can be calculated with the porosity (ε) and the average cross-sectional area of pores $\pi < r_p^2 >$ as input parameters. The tortuosity parameter of a disordered pore network is defined by Eq. 20, and the EMT consequently results in the association between bulk permeability, as shown in Eq. 21. It is the theoretical framework that defines membrane pore size distribution based on the contribution of gas transport.

$$i = \frac{\pi r_p{}^2 K(r_p) D(r_p)}{RTl}(-\Delta p) \tag{15}$$

$$K(r_p) = \frac{2}{r_p^2}\int_0^{r_p - r_s} \exp\left(\frac{-\varphi(r)}{k_B T}\right) r dr \tag{16}$$

$$\lambda = \frac{\pi r_p^2 K(r_p) D(r_p)}{RTl} \tag{17}$$

$$\left\langle \frac{\lambda(r_p) - \lambda e}{\lambda(r_p) + \left(\frac{N}{2} - 1\right)\lambda e} \right\rangle = 0 \tag{18}$$

$$J = \left(\frac{-\varepsilon \lambda_e}{\tau_T \pi \langle r_p{}^2 \rangle}\right) \nabla p \tag{19}$$

$$\tau_T = \frac{3(N+1)}{N-1} \tag{20}$$

$$P = \frac{\varepsilon \lambda_e}{\tau_T \pi \langle r_p{}^2 \rangle RT} \tag{21}$$

2.2.4. Role of structural imperfections in gas transport

In real-world membrane modules, achieving a perfectly selective layer is rare. Small flaws can be attributed to several factors, such as diffusion of dust during the coating, gel contraction during drying, thermal incompatibility during calcination, or stresses generated during sealing [45]. These non-ideal routes, e.g., cracks, pinholes, or sealing-related leaks, present other means for gas to flow across the high-pressure to the low-pressure side [46]. The gas transportation follows the viscous flow model (Eq. 22) when the channels in the membranes are even wider than the mean free path of gases. Knudsen flow is the dominant mode of transport when the characteristic width of these imperfections is smaller than the mean free path of these gas molecules [47], represented in the corresponding Eq. 23. Although Knudsen flow is inherently non-selective compared to molecular sieving, there can be a narrow level of selectivity based on molecular mass. In the current model, the overall measured flux is taken to be a sum of transport contributions by the silica pore network and structural defects [48]:

$$J_{viscous} = -\frac{\varepsilon_p}{\tau_p}\frac{r_p{}^2}{8\eta_v}\frac{p}{RT}\frac{dp}{dz} = -\frac{\varepsilon_p}{\tau_p}\frac{r_p{}^2}{8\eta_v}\frac{p}{RT}\frac{\Delta p}{L} \tag{22}$$

$$J_{Knudsen} = -\frac{2}{3}\frac{\varepsilon_p r_p}{\tau_p}\sqrt{\frac{8}{\pi RTM}}\frac{dp}{dz} = -\frac{2}{3}\frac{\varepsilon_p r_p}{\tau_p}\sqrt{\frac{8}{\pi RTM}}\frac{\Delta p}{L} \tag{23}$$

$$J_{total} = J_{pore} + J_{Knudsen} + J_{viscous} \tag{24}$$

Thus, the temperature dependence of this composite transport mechanism is summarized in the experimentally determined apparent activation energy. This relationship is formalized in Eq. (25), which correlates the measured E_a and cumulative permeation behavior.

$$E_a = \frac{\partial \ln\left(\frac{P}{l}\right)}{\partial(-RT)^{-1}} \tag{25}$$

Due to the difficulty associated with the direct experimental determination of a specific pore size distribution and a defect contribution, an inverse method is used. In particular, the apparent activation energies obtained through gas permeation experiments were used to determine the most likely pore size distribution and assess the defect contributions.

Fig. 3 outlines the iterative modeling process where pore size distribution and Knudsen flow contribution are optimized in an iterative procedure until the corresponding apparent activation energy matches empirical results. The oscillator model was used to compute the apparent activation energy per single pore, as shown in Table 5. The

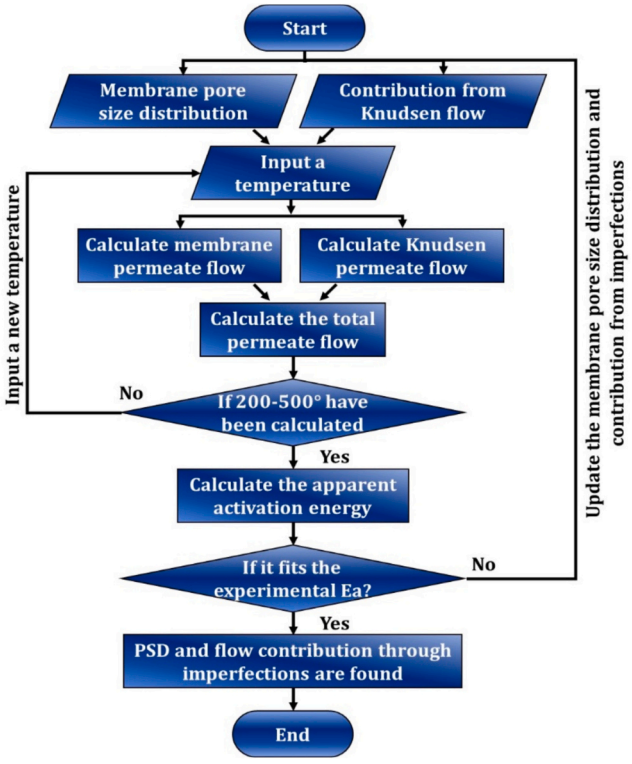

Fig. 3. Schematic overview of the modeling framework.

data shows that in the 5-membered ring, the E_a of both gases are positive with considerably large values of N_2. In the six-membered ring, He has a negative value, while N_2 shows a positive value, indicating a transition in the dominant transport mechanism with increasing pore size. This difference in the magnitude and sign of the apparent activation energy with varying sizes of the rings is in agreement with the fact that gas permeation must be occurring through pores of more than one characteristic dimension, thus providing direct evidence of portraying a pore size distribution.

The pore network here is modeled by a supposed population of 5,000,000 pores grouped in 5–9-membered ring families, which enabled estimating a hypothesized pore size distribution. By using the hypothesized distribution, the gas permeance at a given temperature was calculated according to Eq. 19 with the associated network permeability. This permeance was then determined at various temperatures, and the apparent activation energy was determined using Eq. 11. The E_a calculated was then compared with the experimentally obtained E_a. Concurrently, experimental data of gas permeance at different temperatures were also compared with those calculated. When there was a significant difference between calculated and experimental values, the pore distribution was readjusted, and the calculation was reiterated. On the other hand, when the deviation was sufficiently small and the mismatch in E_a was negligible, the respective pore size distribution was considered representative of the membrane structure. To consider both He and N_2 at the same time, an error metric e_{Total} was used as follows:

$$e_{Total} = \frac{\left|E_{a,mod}^{N_2} - E_{a,exp}^{N_2}\right|}{\left|E_{a,exp}^{N_2}\right|} + \frac{\left|E_{a,mod}^{He} - E_{a,exp}^{He}\right|}{\left|E_{a,exp}^{He}\right|} \quad (26)$$

where modeled and experimental activation energies for He and N_2 are denoted $E_{a,mod}^{He}$, $E_{a,mod}^{N2}$, and $E_{a,exp}^{He}$, $E_{a,exp}^{N}{}^{2}$, respectively. The estimated pore size distribution with minimum e_{Total} was selected as the most representative of the actual membrane structure.

3. Results and discussion

3.1. Gas permeance of evaporation-dried and freeze-dried Co-silica membranes

The temperature-dependent single-gas permeance of He and N_2 for both evaporation-dried and freeze-dried Co-silica membranes is summarized in Table 6. For both membranes, He permeance increased steadily with temperature from 200 to 500 °C, indicating thermally activated transport through the microporous silica network. Permeance of He in the evaporation-dried membrane increased to 6.20×10^{-7}, with a relatively weak temperature dependence of N_2 permeance with only a small rise over the same temperature range. Conversely, the freeze-dried membrane had significantly lower permeance values of both gases at all temperatures, with He permeance rising from 1.98×10^{-8} to 9.14×10^{-8}, whereas N_2 permeance was nearly two orders of magnitude lower than that of He. The difference in the values of permeance between He and N_2 was much higher for the freeze-dried membrane, which corresponds to greater size-selective transport. These patterns of permeance allow the experimental foundation of future analysis of apparent activation energies, which further clarify the underlying pore structure and the dominant transport mechanisms in each type of membrane.

Table 5
Pore-size-dependent gas permeation activation energies (kJ mol^{-1}) of He and N_2.

	E_a (He)	E_a (N_2)
5-membered ring	21.6	843.3
6-membered ring	−1.5	117.6
7-membered ring	−4.5	−4.8
8-membered ring	−4.5	−21.6
9-membered ring	−4	−20.2

Table 6
Gas permeance of evaporation-dried and freeze-dried Co-silica membranes.

Temperature (°C)	Permeance (mol m^{-2} s^{-1} Pa^{-1})			
	Evaporation-dried membrane		**Freeze-dried membrane**	
	He	**N_2**	**He**	**N_2**
200	$2.42 \times 10^{-7} \pm 7.26 \times 10^{-9}$	$7.12 \times 10^{-8} \pm 1.54 \times 10^{-9}$	$1.98 \times 10^{-8} \pm 5.94 \times 10^{-10}$	$6.75 \times 10^{-10} \pm 1.10 \times 10^{-11}$
300	$2.95 \times 10^{-7} \pm 8.85 \times 10^{-9}$	$7.37 \times 10^{-8} \pm 1.42 \times 10^{-9}$	$3.77 \times 10^{-8} \pm 1.13 \times 10^{-9}$	$9.13 \times 10^{-10} \pm 1.97 \times 10^{-11}$
400	$4.50 \times 10^{-7} \pm 1.35 \times 10^{-8}$	$8.45 \times 10^{-8} \pm 1.55 \times 10^{-9}$	$6.37 \times 10^{-8} \pm 1.91 \times 10^{-9}$	$1.09 \times 10^{-9} \pm 1.19 \times 10^{-11}$
500	$6.20 \times 10^{-7} \pm 1.86 \times 10^{-8}$	$8.60 \times 10^{-8} \pm 1.17 \times 10^{-9}$	$9.14 \times 10^{-8} \pm 2.74 \times 10^{-9}$	$1.50 \times 10^{-9} \pm 1.73 \times 10^{-11}$

3.2. Apparent E_a of evaporation-dried and freeze-dried Co-silica membranes

The apparent E_a calculated from experimental permeation data and mathematical modeling is graphically compared in Fig. 4. Both membranes fabricated by evaporation and freeze-drying exhibited the expected trend of activation energies, with N_2 showing a considerably lower E_a as compared to He, reflecting its higher polarizability and stronger gas surface interactions. Both evaporation-dried and freeze-dried membranes exhibit strong consistency in the apparent E_a that are obtained both experimentally and by modeling. In the case of evaporation-dried membrane, the modeled E_a values (9687.6 J mol^{-1} in the case of He, and 2128.7 J mol^{-1} in the case of N_2) are in perfect statistical agreement with the experimental values of 9598.2 J mol^{-1} and 2128.7 J mol^{-1}, respectively. An equally close correlation can also be identified in the case of freeze-dried membrane, where the modeled E_a values (15,522 J mol^{-1} of He, and 7700.9 J mol^{-1} of N_2) are well in accord with the experimental values of 15,579.7 J mol^{-1} and 7700.9 J mol^{-1}. The differences between modeled and experimental values in both membranes were within a negligible range, clearly indicating that the activated transport model is highly reliable in predicting the transport resistance of He and N_2 permeation. In general, the statistical consistency of the modeled and experimental values of E_a shows the effectiveness of the modeling method and confirms its applicability to membranes fabricated through evaporation drying and freeze-drying methods (See Fig. 4).

The pore size distribution estimated using the apparent activation energies shows that there are notable structural variations between the evaporation-dried and freeze-dried Co-silica membranes. In both membranes, small rings dominated the formation of the network, but the smaller pores are more concentrated in the freeze-dried membrane, as demonstrated in Fig. 5. In the evaporation-dried membrane, 5- and 6-membered rings contribute approximately 66.1% and 31.8% of the total population, respectively; the rest are distributed among 7-, 8-, and 9-membered rings at insignificant but appreciable levels. In contrast, the freeze-dried membrane has an even greater contribution of 5- and 6-membered rings, which are 66.6% and 31.9% of the total population, respectively, and the percentage of 7-, 8-, and 9-membered rings declined accordingly. Thus, the obtained results suggest that freeze drying forms a more densely packed, microporous network, where transport is dominated by the smaller siloxane rings, as compared to evaporation drying, which gives a more extensive pore-size distribution with a marginally higher contribution shifted toward larger rings. The compact pore structure observed in freeze-dried membranes can be attributed to the fact that the capillary stresses are inhibited during the

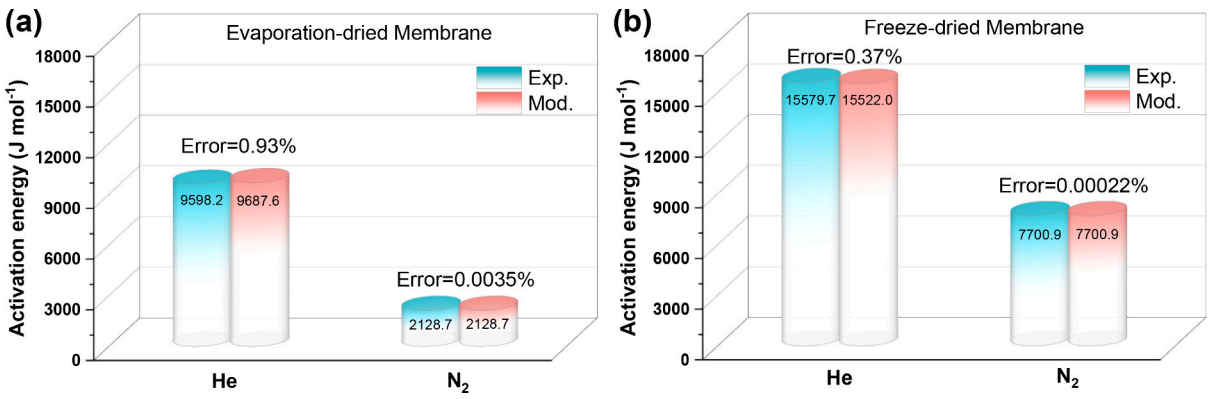

Fig. 4. Comparison of modeled apparent activation energy to the experimental apparent activation energy of (a) evaporation-dried membrane and (b) freeze-dried membrane.

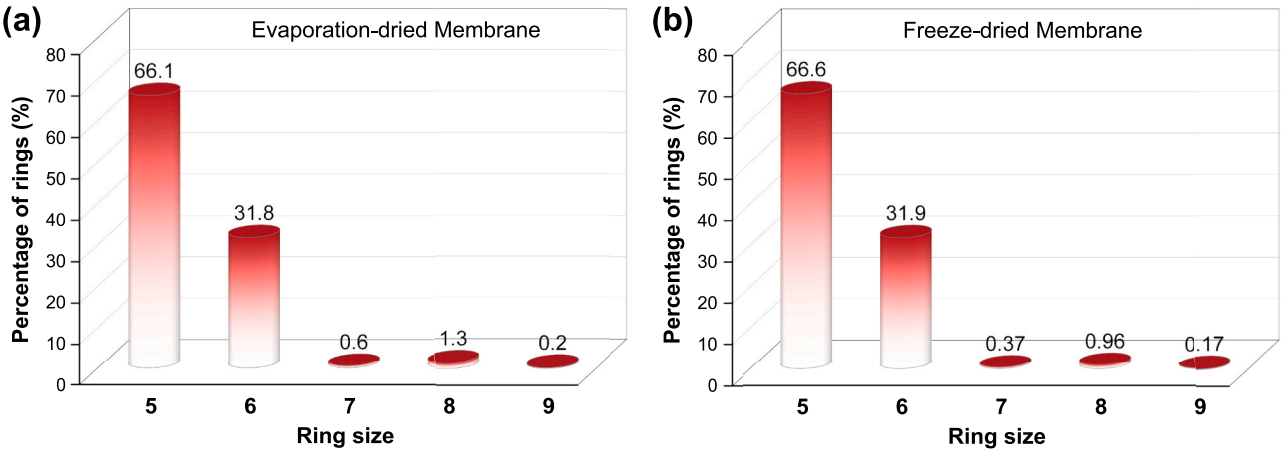

Fig. 5. Pore size distribution (PSD) of (a) evaporation-dried membrane and (b) freeze-dried membrane.

removal of the solvent. When using the conventional evaporation drying method, liquid-vapor interfaces arise within the gel pores during the process of solvent evaporation. The interfaces create capillary pressure, which may cause significant mechanical stress in the silica gel network. Freeze-drying, on the other hand, eliminates the solvent through the sublimation of frozen solvent crystals, thus preventing the development of liquid-vapor interfaces during the drying process. Consequently, the capillary pressure on the silica framework is considerably decreased, which enables the gel network to maintain its original structure. This preservation of the silica matrix promotes the formation of a more uniform microporous structure and reduces the probability of defect formation.

3.3. Gas transport through imperfections

The transport model presented here was developed to consider a number of potential transport mechanisms, such as activated diffusion, Knudsen diffusion, and viscous (Poiseuille) flow. Macroscopic defects or sealing imperfections would be considered as a measurable viscous flow contribution due to the presence of large transport channels. During the iterative fitting of the permeance data, the viscous flow coefficient always converged to zero, representing that the experimental permeance behavior can be explained without considering macroscopic defect pathways. To evaluate the relative contribution of Knudsen diffusion within the overall transport mechanism, the Knudsen coefficient was determined from the model. For both membranes, the contribution of the Knudsen diffusion to the overall transport is minimal. For the evaporation-dried membrane, the Knudsen coefficient is approximately 1.0×10^{-4}, whereas for the freeze-dried membrane, it is even reduced to 1.0×10^{-5}, indicating a one order of magnitude reduction in the relative contribution of Knudsen transport. This reduction indicates the suppression of transport through larger pore openings, and is consistent with the activation energy and permeance data. Furthermore, the temperature-dependent permeance data exhibited activated transport properties, demonstrating that the gas transport is dominated by diffusion through the intrinsic microscopic silica structure. Collectively, these results indicate that the freeze-drying method, by eliminating the capillary stresses, generated a membrane with tighter diffusion pathways, increased dominance of activated transport, and less non-selective Knudsen flow than the evaporation-dried method.

3.4. Gas permeance of evaporation-dried and freeze-dried Co-silica membranes

The experimental permeance of both membranes is well-matched with the predicted permeance trends based on reconstructed pore-size distributions (Fig. 6). In the evaporation-dried membrane, closely matched experimental and modeled permeances of He and N_2 throughout the entire temperature range validate that the differences in the size of rings, especially the larger pore sizes, were well represented in the pore-size distribution. Likewise, in the freeze-dried membrane, the close modeled and experimental He and N_2 permeances indicate the prevalence of small rings within this membrane, further confirming that the compact pore network obtained by activation-energy analysis is physically feasible. The high consistency between experimental and modeled permeances confirms that the calculated pore-size distributions

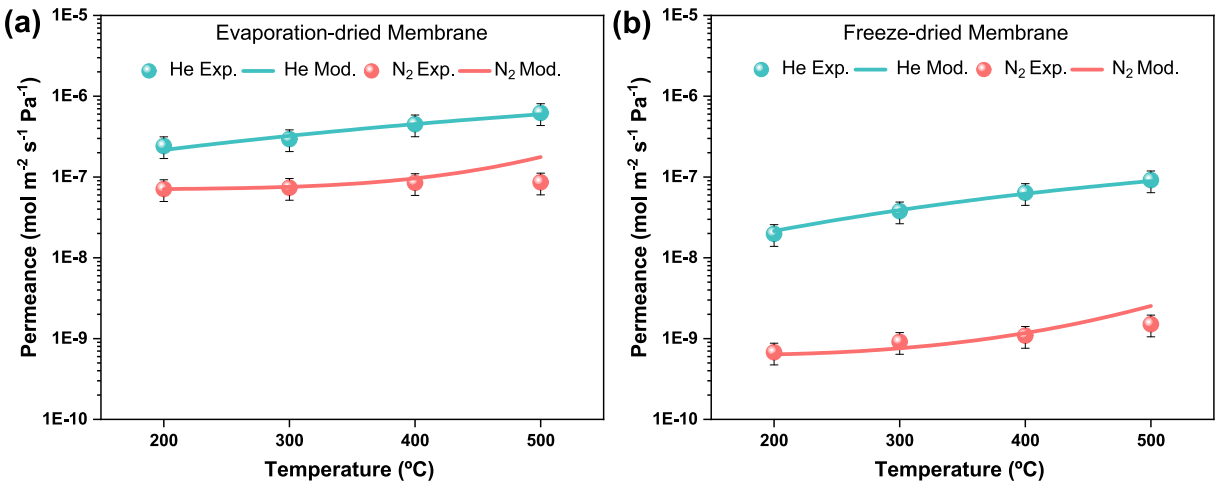

Fig. 6. Comparison of modeled permeance to the experimental permeance of (a) evaporation-dried membrane and (b) freeze-dried membrane.

are accurate and that the structural difference between evaporation-dried and freeze-dried membranes was appropriately modeled.

3.5. Sensitivity of 5-membered rings in Co-silica membranes

Interestingly, the tenfold reduction in Knudsen coefficient of freeze-dried membranes, despite their nearly similar pore size distribution to evaporation-dried membranes, resulted in gas permeation differences exceeding one order of magnitude. This behavior is consistent with the gas transport in sub-nanometer silica membranes, which is highly sensitive to small shifts in the balance between 5 and 6-membered rings population. To examine this sensitivity, a systematic analysis was conducted by fixing the number of 7-, 8-, and 9-membered rings, the Knudsen coefficient, and the pore connectivity value of each gas and only varying the population of 5- and 6-membered rings. Both evaporation-dried and freeze-dried membranes showed identical sensitivity curves for each gas.

As illustrated in Fig. 7, the E_a of He (Fig. 7a) and N_2 (Fig. 7b) exhibited a pronounced non-linear dependence on the number of 5-membered rings. Importantly, the relevant 5-membered ring populations of the evaporation-dried (66.1%) and freeze-dried (66.6%) membranes fall within the steep transition region of these sensitivity curves. In this region, small shifts in the balance of 5/6-membered rings cause significant changes in the activation energy. Even with the only 0.6% difference in the combined fraction of the 5–6-membered rings between the two membranes, the localization of each of the membranes within this super-sensitive regime provides greatly different activation energies and permeance values. These results indicate that the gas transport becomes super-responsive to small shifts in the population of the dominant ring structures when the pore network lies in the sensitive region. Therefore, membranes with pore-size distributions that closely resemble each other can still have significantly different transport characteristics.

4. Conclusions

This paper successfully integrated experimental results of gas permeation with an activation-energy-based modeling framework to quantitatively clarify the difference in pore size distribution of amorphous silica membranes synthesized by traditional evaporation drying and novel freeze drying. Directly correlating apparent activation energy with siloxane ring populations gave a powerful structure-transport relationship that was not dependent on membrane thickness or the traditional limitations of pore characterization. Modeled and experimental activation energies were statistically compared, and excellent agreement was obtained in both types of membranes. In the case of the evaporation-dried membrane, the modeled E_a values of He (9687.6 J mol^{-1}) and N_2 (2128.7 J mol^{-1}) were close to the experimental values of 9598.2 J mol^{-1} and 2128.7 J mol^{-1}, respectively. Likewise, the freeze-dried membrane had strong consistency, where modeled E_a values of

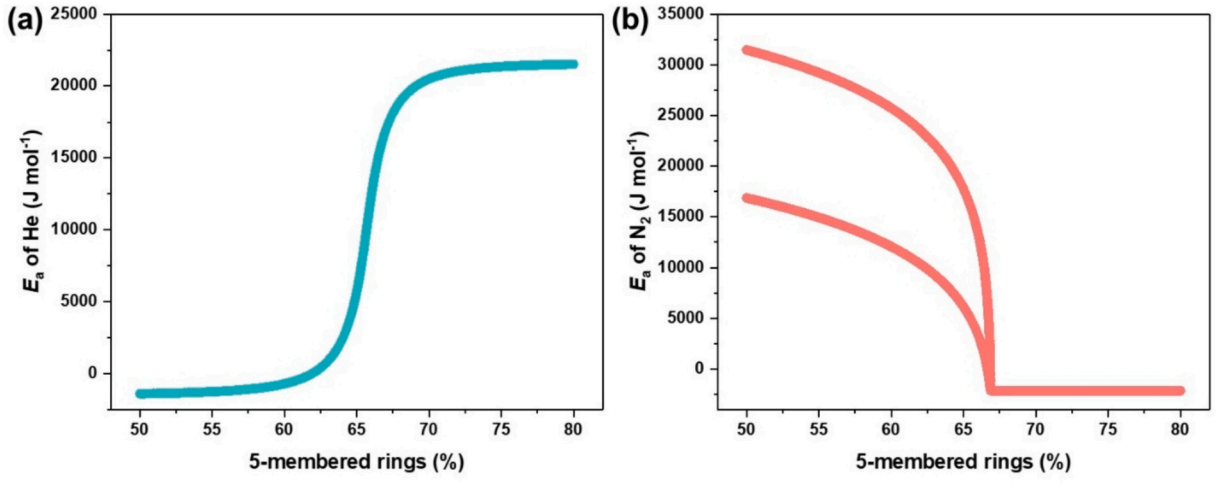

Fig. 7. The E_a of (a) He and (b) N_2 as a function of the number of 5-membered rings obtained from sensitivity analysis.

15,522.0 J mol^{-1} (He) and 7700.9 J mol^{-1} (N_2) were close to the experimental values of 15,579.7 J mol^{-1} and 7700.9 J mol^{-1}. These findings confirm that the activated transport model is effective in describing the inherent activation thresholds that govern gas permeation in both membranes. Determination of the pore size distribution showed clear structural variations in both membranes caused by the different drying method. The evaporation-dried membrane had a larger pore size distribution, with about 97.9% 5- and 6-membered rings. By contrast, the freeze-dried membrane exhibited a more compact pore structure comprising a higher percentage of smaller 5- and 6-membered rings (98.5%), with fewer 7- to 9-membered rings than the evaporation-dried membrane. This structural refinement was directly mapped into transport behavior, which is verified by permeance validation. In general, the present work shows that freeze drying can be successfully used to reduce structural defects caused by surface tension to produce more uniform and compact silica membranes with better pore size control. The model provides a physically meaningful framework to interpret and relate membrane structure to transport behavior, and it provides structural bases for predicting relative separation performance. Furthermore, the presented activation-energy-based method represents a powerful and widely applicable methodology to determine pore size distribution in sub-nanometer membrane systems, which is of valuable guidance in the rational design of high-performance silica membrane systems for the H_2 separation and membrane reactor applications.

CRediT authorship contribution statement

Tanzila Anjum: Writing – original draft, Formal analysis, Investigation, Data curation, Methodology. **Tian Heng Qin:** Methodology, Formal analysis. **Gianni Olguin:** Writing – review & editing. **Yinxiang Wang:** Methodology. **Dongkuan Zhang:** Methodology. **Xiaonan Kou:** Methodology. **David K. Wang:** Writing – review & editing. **Xiaozhen Zhang:** Writing – review & editing. **Bradley Ladewig:** Writing – review & editing. **Asim Laeeq Khan:** Writing – review & editing. **Guozhao Ji:** Conceptualization, Resources, Supervision, Funding acquisition, Project administration, Writing – review & editing.

Declaration of competing interest

The authors declare that they have no known competing financial interests or personal relationships that could have appeared to influence the work reported in this paper.

Acknowledgments

The authors gratefully acknowledge the financial support from the National Key Research and Development Program of China [2025YFE0109700].

Data availability

Data will be made available on request.

References

[1] Z. Zhang, T. Anjum, Y. Wang, Y. Meng, T. Qin, Y.S. Zhang, Y. Zhang, A. Li, G. Ji, Hydrogen production from biomass waste gasification under the enhancement of catalyst-sorbent hybrid functional material synthesized from steel slag, Chin. J. Chem. Eng. 88 (2025) 108–123.
[2] T. Zhao, J. Tan, W. Zhou, Z. Gu, Y. Niu, Z. Liu, G. Zhang, W. Jin, Engineering robust porous/dense composite hollow fiber membranes for highly efficient hydrogen separation, J. Membr. Sci. 705 (2024) 122872.
[3] H.-C. Wu, Z. Rui, J.Y. Lin, Hydrogen production with carbon dioxide capture by dual-phase ceramic-carbonate membrane reactor via steam reforming of methane, J. Membr. Sci. 598 (2020) 117780.
[4] G. Ji, X. Kou, G. Olguin, T. Anjum, X. Yin, Y. Guo, B. Qu, Enhanced hydrogen production from ammonia decomposition by a silica membrane reactor, Sep. Purif. Technol. 379 (2025) 134989.
[5] H. Wang, X. Dong, Y. Lin, Membrane Reactors for Hydrogen Production from Coal, in: Membrane Reactors for Energy Applications and Basic Chemical Production, Elsevier, 2015, pp. 145–186.
[6] D.K. Wang, J. Motuzas, J.C.D. da Costa, S. Smart, Rapid thermal processing of tubular cobalt oxide silica membranes, Int. J. Hydrog. Energy 38 (18) (2013) 7394–7399.
[7] G. Ji, X. Yin, W. Fu, X. Kou, D. Hotza, Y. Wang, A. Li, G. Olguin, W. Wang, Enhancement of hydrogen clean energy production from greenhouse gas by in-situ hydrogen separation with a cobalt-silica membrane, J. Clean. Prod. 388 (2023) 135874.
[8] J.Y. Lin, Inorganic membranes: past, present, challenges and future perspective, Sep. Purif. Technol. 377 (2025) 134405.
[9] T. Tsuru, Nano/subnano-tuning of porous ceramic membranes for molecular separation, J. Sol-Gel Sci. Technol. 46 (3) (2008) 349–361.
[10] A. Darmawan, J. Motuzas, S. Smart, A. Julbe, J.C.D. da Costa, Binary iron cobalt oxide silica membrane for gas separation, J. Membr. Sci. 474 (2015) 32–38.
[11] P. Karakiliç, C. Huiskes, M.W. Luiten-Olieman, A. Nijmeijer, L. Winnubst, Sol-gel processed magnesium-doped silica membranes with improved H2/CO2 separation, J. Membr. Sci. 543 (2017) 195–201.
[12] G. Ji, J.G. Yao, P.T. Clough, J.C.D. Da Costa, E.J. Anthony, P.S. Fennell, W. Wang, M. Zhao, Enhanced hydrogen production from thermochemical processes, Energy Environ. Sci. 11 (10) (2018) 2647–2672.
[13] V. Bui, A.M. Tandel, V.R. Satti, E. Haddad, H. Lin, Engineering silica membranes for separation performance, hydrothermal stability, and production scalability, Adv. Membranes 3 (2023) 100064.
[14] S. Aoyama, H. Nagasawa, N. Moriyama, K. Ito, T. Tsuru, M. Kanezashi, Ultrathin highly porous molecular-sieve silica membranes developed by a facile process using atmospheric-pressure plasma modification, ACS Materials Letters 7 (9) (2025) 3058–3064.
[15] I. Myronyuk, V. Kotsyubynsky, T. Dmytrotsa, L. Soltys, V. Gun'Ko, Atomic structure and morphology of fumed silica, Phys. Chem. Solid State 21 (2) (2020) 325–331.
[16] T. Uchino, Y. Tokuda, T. Yoko, Vibrational dynamics of defect modes in vitreous silica, Physical Review B - Condensed Matter and Materials Physics 58 (9) (1998) 5322–5328, https://doi.org/10.1103/PhysRevB.58.5322.
[17] P.G. Coombs, J.F. De Natale, P.J. Hood, D.K. McElfresh, R.S. Wortman, J. F. Shackelford, The nature of the Si-O-Si bond angle distribution in vitreous silica, philosophical magazine B: physics of condensed matter; Statistical Mechanics, Electronic, Optical and Magnetic Properties 51 (4) (1985) 39–42, https://doi.org/10.1080/13642818508240582.
[18] T. Uchino, Structure and properties of amorphous silica and its related materials: recent developments and future directions, J. Ceram. Soc. Jpn. 113 (1313) (2005) 17–25, https://doi.org/10.2109/jcersj.113.17.
[19] G. Ji, X. Gao, S. Smart, S.K. Bhatia, G. Wang, K. Hooman, J.C. Diniz da Costa, Estimation of pore size distribution of amorphous silica-based membrane by the activation energies of gas permeation, Processes 6 (12) (2018) 239.
[20] P. Hacarlioglu, D. Lee, G. Gibbs, S. Oyama, Activation energies for permeation of he and H2 through silica membranes: an ab initio calculation study, J. Membr. Sci. 313 (1–2) (2008) 277–283.
[21] D.K. Wang, J.C.D. da Costa, S. Smart, Development of rapid thermal processing of tubular cobalt oxide silica membranes for gas separations, J. Membr. Sci. 456 (2014) 192–201.
[22] L. Wang, J. Yang, R. Mu, Y. Guo, H. Hou, Sol-gel processed cobalt-doped methylated silica membranes calcined under N2 atmosphere: microstructure and hydrogen perm-selectivity, Materials 14 (15) (2021) 4188.
[23] T. Breinlinger, A. Hashibon, T. Kraft, Simulation of the influence of surface tension on granule morphology during spray drying using a simple capillary force model, Powder Technol. 283 (2015) 1–8.
[24] L. Manzocco, S. Plazzotta, J. Powell, A. de Vries, D. Rousseau, S. Calligaris, Structural characterisation and sorption capability of whey protein aerogels obtained by freeze-drying or supercritical drying, Food Hydrocoll. 122 (2022) 107117.
[25] T. Anjum, H. Saulat, G. Olguin, D.K. Wang, X. Zhang, X. Kou, X. Yin, A.L. Khan, G. Ji, Surface-tension-free fabrication to minimize defects in cobalt-silica membranes via freeze drying technique for H2 separation at high temperatures, J. Mater. Chem. A 14 (2026) 1946–1959.
[26] K.K. Abla, M.M. Mehanna, Freeze-drying as a tool for preparing porous materials: from proof of concept to recent pharmaceutical applications, AAPS PharmSciTech 26 (5) (2025) 159.
[27] L. Qian, H. Zhang, Controlled freezing and freeze drying: a versatile route for porous and micro−/nano-structured materials, J. Chem. Technol. Biotechnol. 86 (2) (2011) 172–184.
[28] K. Sing, The use of nitrogen adsorption for the characterisation of porous materials, Colloids Surf. A Physicochem. Eng. Asp. 187 (2001) 3–9.
[29] T. Tsuru, T. Hino, T. Yoshioka, M. Asaeda, Permporometry characterization of microporous ceramic membranes, J. Membr. Sci. 186 (2) (2001) 257–265.
[30] M.C. Duke, S.J. Pas, A.J. Hill, Y. Lin, J.C.D. Da Costa, Exposing the molecular sieving architecture of amorphous silica using positron annihilation spectroscopy, Adv. Funct. Mater. 18 (23) (2008) 3818–3826.
[31] G. Olguin, C. Yacou, J. Motuzas, M. Butterling, W.A. Meulenberg, S. Smart, J.C. D. da Costa, Surfactant functionalised cobalt silica membranes–gas permeation and thin film positron annihilation lifetime spectroscopy characterisation, J. Membr. Sci. 664 (2022) 121040.
[32] T. Yoshioka, T. Tsuru, M. Asaeda, Molecular dynamics study of gas permeation through amorphous silica network and inter-particle pores on microporous silica membranes, Mol. Phys. 102 (2) (2004) 191–202.

[33] M. Kanezashi, T. Sasaki, H. Tawarayama, H. Nagasawa, T. Yoshioka, K. Ito, T. Tsuru, Experimental and theoretical study on small gas permeation properties through amorphous silica membranes fabricated at different temperatures, J. Phys. Chem. C 118 (35) (2014) 20323–20331.
[34] X. Kou, T. Anjum, K. Sun, L. Liu, G. Ji, A.L. Khan, M. Elma, G. Olguin, Insights into the pore size distribution of amorphous silica membranes using gas permeation activation energies, J. Membr. Sci. 713 (2025) 123269.
[35] G. Ji, X. Kou, T. Anjum, A.L. Khan, X. Yin, M. Elma, G. Olguin, The interpretation of diverging hydrogen and carbon dioxide permeations with temperature across silica-based membranes, J. Membr. Sci. 695 (2024) 122472.
[36] S. Battersby, M.C. Duke, S. Liu, V. Rudolph, J.C.D.D. Costa, Metal doped silica membrane reactor: operational effects of reaction and permeation for the water gas shift reaction, J. Membr. Sci. 316 (1–2) (2008) 46–52, https://doi.org/10.1016/j.memsci.2007.11.021.
[37] R.S.A. de Lange, J.H.A. Hekkink, K. Keizer, A.J. Burggraaf, Formation and characterization of supported microporous ceramic membranes prepared by sol-gel modification techniques, J. Membr. Sci. 99 (1) (1995) 57–75, https://doi.org/10.1016/0376-7388(94)00206-E.
[38] A.W. Thornton, T. Hilder, A.J. Hill, J.M. Hill, Predicting gas diffusion regime within pores of different size, shape and composition, J. Membr. Sci. 336 (1–2) (2009) 101–108.
[39] S.K. Bhatia, Modeling pure gas permeation in nanoporous materials and membranes, Langmuir 26 (11) (2010) 8373–8385.
[40] B. Rodríguez García, M.M. Piñeiro, M. Pérez-Rodríguez, Influence of lennard–jones parameters in the temperature dependence of real gases diffusion through nanochannels, Nanomaterials 13 (9) (2023), https://doi.org/10.3390/nano13091534.
[41] S.K. Bhatia, D. Nicholson, Hydrodynamic origin of diffusion in nanopores, Phys. Rev. Lett. 90 (1) (2003) 016105, https://doi.org/10.1103/PhysRevLett.90.016105.
[42] M.R. Bonilla, S.K. Bhatia, The low-density diffusion coefficient of soft-sphere fluids in nanopores: accurate correlations from exact theory and criteria for applicability of the Knudsen model, J. Membr. Sci. 382 (1–2) (2011) 339–349, https://doi.org/10.1016/j.memsci.2011.08.033.
[43] S.K. Bhatia, O. Jepps, D. Nicholson, Tractable molecular theory of transport of Lennard-Jones fluids in nanopores, J. Chem. Phys. 120 (9) (2004) 4472–4485, https://doi.org/10.1063/1.1644108.
[44] X. Gao, J.C. Diniz da Costa, S.K. Bhatia, Adsorption and transport of gases in a supported microporous silica membrane, J. Membr. Sci. 460 (2014) 46–61, https://doi.org/10.1016/j.memsci.2014.02.028.
[45] S.P. Cardoso, I.S. Azenha, Z. Lin, I. Portugal, A.E. Rodrigues, C.M. Silva, Inorganic membranes for hydrogen separation, Sep. Purif. Rev. 47 (3) (2018) 229–266.
[46] Z. Wu, Inorganic Membranes for Gas Separations, in: Membrane Separation Principles and Applications, Elsevier, 2019, pp. 147–179.
[47] Y.T. Chua, G. Ji, G. Birkett, C.X.C. Lin, F. Kleitz, S. Smart, Nanoporous organosilica membrane for water desalination: theoretical study on the water transport, J. Membr. Sci. 482 (2015) 56–66.
[48] C. Yacou, S. Smart, J.C.D. da Costa, Long term performance cobalt oxide silica membrane module for high temperature H 2 separation, Energy Environ. Sci. 5 (2) (2012) 5820–5832.